Impact of current-wind interaction on vertical processes in the Southern Ocean

Hajoon Song[1], John Marshall[2], Dennis J. McGillicuddy Jr.[3] and Hyodae Seo[4]

[1]Department of Atmospheric Sciences, Yonsei University

[2]Department of Earth, Atmospheric and Planetary Sciences, Massachusetts Institute of Technology

[3]Applied Ocean Physics & Engineering, Woods Hole Oceanographic Institution

[4]Physical Oceanography Department, Woods Hole Oceanographic Institution

Key Points:

- High resolution Southern Ocean simulations suggest that current-wind-stress interaction on the mesoscale reduces eddy kinetic energy by 25%.
- Current-wind interaction induces a net upward linear but downward nonlinear modulation of Ekman pumping rates.
- Current-wind interaction enhances stratification near the bottom of the mixed layer by up to 10%.

Corresponding author: Hajoon Song, `hajsong@yonsei.ac.kr`

Abstract

Momentum input from westerly winds blowing over the Southern Ocean can be modulated by mesoscale surface currents and result in changes in large-scale ocean circulation. Here, using an eddy-resolving 1/20 degree ocean model configured near Drake Passage, we evaluate the impact of current-wind interaction on vertical processes. We find a reduction in momentum input from the wind, reduced eddy kinetic energy, and a modification of Ekman pumping rates. Wind stress curl resulting from current-wind interaction leads to net upward motion, while the nonlinear Ekman pumping term associated with horizontal gradients of relative vorticity induces net downward motion. The spatially-averaged mixed-layer depth estimated using a density criteria is shoaled slightly by current-wind interaction. Current-wind interaction, on the other hand, enhances the stratification in the thermocline below the mixed layer. Such changes have the potential to alter biogeochemical processes including nutrient supply, biological productivity and air-sea carbon dioxide exchange.

Plain Language Summary

Momentum transfer between winds blowing over the Southern Ocean depends on the relative speed of the winds and surface currents. Mesoscale eddies with a scale of 100 km or less are very vigorous and thus can modulate momentum transfer. Here, we use an ocean model with sufficiently high horizontal resolution that it can resolve the mesoscale and hence capture the modulation. We find a reduction in the momentum transfer from the wind to the ocean and a reduction in eddy kinetic energy, together with a modification of wind-driven vertical motion. Structural changes in the wind stress field modify patterns of upwelling and downwelling in a manner that can be understood from nonlinear Ekman theory. Moreover, current-wind interaction results in an increase in the stratification below the mixed layer and hence a reduced communication between the surface and the interior ocean. There is thus a potential impact on biogeochemical processes and the climate of the Southern Ocean.

1 Introduction

Both satellite observations and atmospheric reanalyses show the world's strongest winds blow over the Southern Ocean (Tsujino et al., 2018). Underneath, and driven by the westerly winds, flows an ocean current directed generally eastward with speeds of

46 several tens of cm s^{-1} (Maximenko et al., 2009; Dohan & Maximenko, 2010; Laurindo

47 et al., 2017). This Antarctic Circumpolar Current (ACC) circumnavigates the globe pass-

48 ing through Drake Passage near 60°S (Talley et al., 2011). While both winds and cur-

49 rents generally flow eastward, the wind blows faster than the currents and so there is a

50 continuous transfer of momentum from the wind to the ocean. The stress $\boldsymbol{\tau} = (\tau_x, \ \tau_y)$

51 at the surface is given by:

$$\boldsymbol{\tau} \quad = \quad \rho_a C_D \left(\mathbf{u}_a - \mathbf{u}_o\right) |\mathbf{u}_a - \mathbf{u}_o|, \tag{1}$$

52 where $(\mathbf{u}_a = (u_{a,x}, \ u_{a,y}))$ is the 10 m wind, $(\mathbf{u}_o = (u_{o,x}, \ u_{o,y}))$ is the surface current,

53 and ρ_a, C_D are the air density and drag coefficient, respectively (Large & Yeager, 2004).

54 The 10-m wind is the main source of wind stress variability because winds have shorter

55 timescales than ocean currents, especially in the storms blowing over the ACC. Often

56 the effect of ocean currents on the surface stress is neglected because $|\mathbf{u}_a| \gg |\mathbf{u}_o|$. How-

57 ever, in turbulent oceanic regimes such as the Southern Ocean, where the spatial scale

58 of the surface currents is much shorter than that of the wind, this assumption must be

59 reevaluated: the wind stress and its curl can be significantly affected by the presence of

60 the ocean's mesoscale.

61   The prevailing westerly wind leads to equatorward Ekman transport and upwelling

62 to the south of the ACC. As a result, isopycnals shoal and the ocean gains available po-

63 tential energy. This is then converted to eddy kinetic energy via baroclinic instability

64 resulting in the ubiquitous meanders and mesoscale eddies typical of the ACC. These

65 mesoscale features constantly change the direction of the flow, leaving imprints on the

66 wind stress field through Eq.(1), such that the wind stress increases/decreases when the

67 ocean flows in the opposite/same direction of the wind. This occurs on spatial scales char-

68 acterized by the first baroclinic Rossby radius of deformation which is generally less than

69 30 km along the ACC (Chelton et al., 1998; Tulloch et al., 2011). In the special case of

70 mesoscale eddies possessing vorticity over which a uniform wind without vorticity blows,

71 one "side" of the ocean eddy has enhanced stress relative to the other. This "top drag"

72 effect (Dewar & Flierl, 1987) dampens mesoscale eddies (Duhaut & Straub, 2006; Dawe

73 & Thompson, 2006; Eden & Dietze, 2009; Zhai et al., 2012). This current-wind inter-

74 action, also known as the effect of "relative wind stress", is believed to dampen mesoscale

75 eddies in many parts of the world's oceans. For example, in modeling and observational

76 studies, the eddy kinetic energy (EKE) can be decreased by 10% in the northwest At-

77 lantic Ocean (Zhai & Greatbatch, 2007), 25% in the Arabian Sea (Seo, 2017) and the

Agulhas Current (Renault, McWilliams, & Penven, 2017), 30% in the Gulf Stream (Renault, Molemaker, Gula, et al., 2016), approximately 50% in the California Current System (Seo et al., 2016; Renault, Molemaker, McWilliams, et al., 2016), and even by as much as 100% in the Bay of Bengal (Seo et al., 2019).

The Southern Ocean is not exceptional in respect to the reduction of EKE through eddy-wind interaction. Hutchinson et al. (2010) report the reduction of kinetic energy in the standing and transient eddies by 11% and 18%, respectively, in their eddy-resolving quasi-geostrophic model driven by a zonally symmetric westerly wind. The reduction of the surface EKE by current-wind interaction is approximately 15% in the idealized channel model experiments reported by Munday and Zhai (2015). They further show that the degree of reduction is sensitive to the total power input by the wind. Current-wind interaction also increases the transport of the ACC and results in steeper isopycnals (Munday & Zhai, 2015). Moreover, satellite observations show that the impact of ocean currents on wind stress is the greatest in the Southern Ocean (Renault, McWilliams, & Masson, 2017).

Although such studies advance our understanding of the impact of ocean current on momentum flux in the Southern Ocean, there are many unanswered questions. Firstly, what is the effect of current-wind interaction on vertical motion? In particular, the Southern Ocean is rich in meanders and eddies, where both linear and nonlinear Ekman pumping contributions are likely to be important. Secondly, can current-wind interaction affect vertical mixing and the stratification of the upper ocean? When wind energy input is reduced by including relative wind stress, one may anticipate a weakening of vertical mixing. However, this effect might be reinforced or offset by changes in stratification in the upper ocean resulting from changes in wind-driven Ekman pumping. Can we parse these effects to arrive at an understanding of the net effect? Furthermore, given that upper ocean stratification and the mixed-layer depth (MLD) exhibit large seasonality (de Boyer Montégut et al., 2004; Dong et al., 2008; Holte & Talley, 2009; Hausmann et al., 2017), we should necessarily focus on the seasonality of the response, which has been absent in previous studies.

In this study, we utilize a high-resolution ocean model in a realistic configuration and investigate current-wind interaction near Drake Passage. Our analysis method is straightforward. We compare two simulations, one with and one without current-wind interac-

110 tion to quantify the effects. Consistent with previous studies, we document a reduction

111 in EKE when the full interaction is included, such that it approaches levels observed from

112 satellite data. The net change of the total Ekman pumping is not significant, but both

113 linear and nonlinear contributions show compensating modifications. Although the mean

114 mixed layer depth is not altered, we observe an increase in the stratification of the up-

115 per thermocline, especially in austral summer.

116 Our study is set out as follows. Section 2 contains a detailed description of the ex-

117 perimental design. The model results are evaluated by computing changes in the wind

118 stress and EKE in section 3. We then analyze changes in the vertical velocity, vertical

119 mixing and stratification in section 4. We conclude in section 5 with a discussion of the

120 results.

2 Experimental Design

122 The effect of current-wind interaction is investigated using the Massachusetts In-

123 stitute of Technology general circulation model (MITgcm) (Marshall, Hill, et al., 1997;

124 Marshall, Adcroft, et al., 1997; A. J. Adcroft et al., 1997; Marshall et al., 1998; A. Ad-

125 croft et al., 2004). The study area includes the Drake Passage and its upstream/downstream

126 regions in the Southern Ocean, covering a 140° longitudinal swath. The ACC snakes through

127 the domain that ranges from 75°S to 35°S (Fig. 1(a)). The horizontal resolution is 0.05°

128 or roughly 4 km along the ACC, enabling us to resolve the mesoscale. The model was

129 integrated for five years driven by the surface atmospheric fields from the Interim Eu-

130 ropean Centre for Medium-Range Weather Forecasts (ECMWF) Re-Analysis 6 hourly

131 data (Simmons et al., 2007) and monthly-mean lateral boundary condition taken from

132 the Ocean Comprehensive Atlas (Forget, 2010). During the simulation, surface heat and

133 freshwater fluxes are computed from bulk formulae (Large & Yeager, 2004), and the 10

134 m wind, neglecting current-wind interaction. Vertical mixing is calculated using the K-

135 profile parameterization (KPP) scheme of Large et al. (1994). KPP first estimates the

136 mixing depth, h, using a Richardson number criterion determined from the surface forc-

137 ing, the vertical buoyancy gradient, and the current shear. The eddy diffusivity is then

138 computed using h, a turbulent velocity scale, and a vertical shape function. This sim-

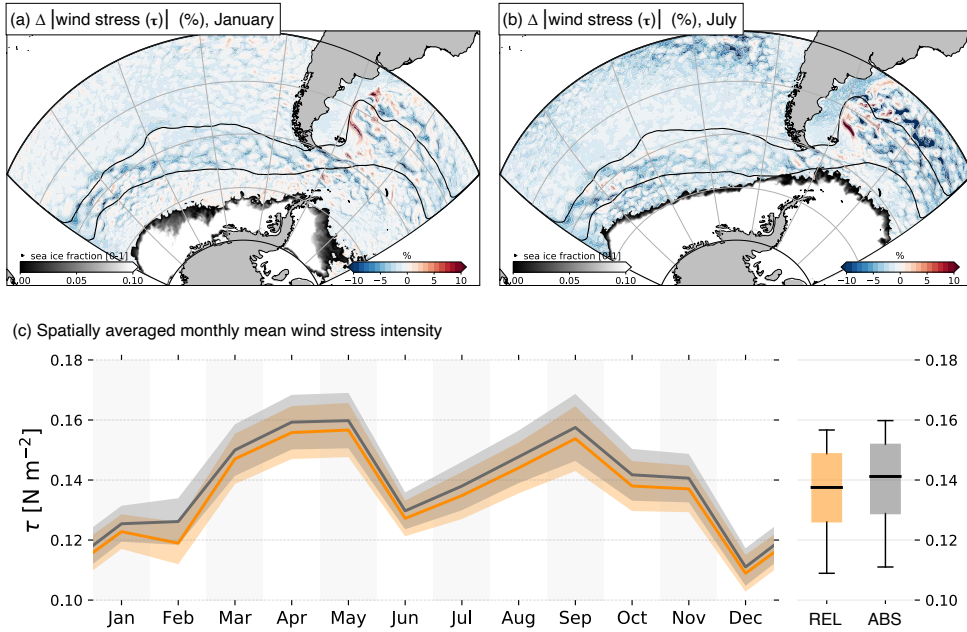139 ulation is referred to as ABS as it uses the absolute wind stress.

Figure 1. Monthly averaged wind stress intensity changes ($\Delta|\tau| = 100 \times (|\tau_{REL}| - |\tau_{ABS}|)/|\tau_{ABS}|$) in (a) January and (b) July. Black solid lines indicate the position of the ACC based on the sea level height. Sea ice fractions are shown in grayscale. Time series of the monthly averaged wind stress intensity along the ACC (marked by black solid lines in (a,b)) in REL and ABS are shown in orange and gray, respectively, in (c). The shading in (c) represents the 95% confidence interval.

This configuration has its root in the simulation of Tulloch et al. (2014) which was thoroughly compared with observations. The 100 vertical levels of the Tulloch configuration were reduced to 50 in which the top 100 m is represented at 10 m resolution. Despite reduced vertical resolution, the 50-level configuration remains qualitatively similar to observations such as EKE and MLD. This configuration has also been successfully coupled with a biogeochemical model for both online (Song et al., 2015, 2016) and offline simulations (Song et al., 2019).

The effect of current-wind interaction is explored by comparing ABS with a simulation in which the wind relative to the surface ocean current is used in the wind stress calculation as in (1). This simulation, referred to as REL, otherwise has the same configuration as ABS and so differences between ABS and REL can be attributed to the current-wind interaction. Simulating ABS and REL at high-resolution is demanding of comput-

¹⁵² ing power, and so we only integrate REL for three and a half years. In REL, EKE is rapidly

¹⁵³ reduced for the first three months, followed by a modest decrease of EKE during the rest

¹⁵⁴ of the integration (not shown). Although the simulations do not necessarily achieve a

¹⁵⁵ statistically-steady state over the three and half year period, it is sufficient for us to an-

¹⁵⁶ alyze the effect of current-wind interactions since the magnitude of the difference in EKE

¹⁵⁷ between REL and ABS does not continue to increase beyond the first few months of sim-

¹⁵⁸ ulation. The first six months were regarded as the spin-up period, and the last three years

¹⁵⁹ of simulation were the focus of our analysis.

3 The impact of current-wind interaction on upper ocean energy

3.1 Wind stress changes

¹⁶² The reduction of wind stress can be anticipated in the Southern Ocean where the

¹⁶³ westerly wind blows over the eastward current. Indeed, the wind stress is reduced in most

¹⁶⁴ of the model domain except in limited areas where the current flows in the opposite di-

¹⁶⁵ rection of the wind (Fig. 1(a,b)). The average reduction is not large (less than 3%) in

¹⁶⁶ both austral summer and winter, although there are regions where the reduction can be

¹⁶⁷ as large as 10% near to the axis of the ACC. The reduction in the wind stress persists

¹⁶⁸ all year round along the ACC, with little sign of a seasonal cycle (Fig. 1(c)). This re-

¹⁶⁹ sult is consistent with previous studies (Hutchinson et al., 2010; Munday & Zhai, 2015)

¹⁷⁰ where the reduction of the wind stress is in the range of 2% to 10%.

¹⁷¹ The reduced eastward wind stress in REL decreases the wind-driven Ekman trans-

¹⁷² port toward the equator. Since the same boundary conditions are applied to both ABS

¹⁷³ and REL, instead of using zonal transport, we analyze the impact of the weaker Ekman

¹⁷⁴ transport on the conversion of the mean potential energy to mean kinetic energy by com-

¹⁷⁵ puting $-g/\rho_0 \int \langle \rho \rangle \langle w \rangle dz$. Although the change is only $O(0.1°)$, the latitudes where isopy-

¹⁷⁶ cnals outcrop in REL are further south than in ABS between 65°S and 45°S (Fig. 2).

¹⁷⁷ This is consistent with Ekman transport being weaker in REL. The conversion from mean

¹⁷⁸ potential energy to mean kinetic energy is less in REL by approximately 3% in the top

¹⁷⁹ 350 m over this latitude band. Despite the small differences, reduced energy conversion

¹⁸⁰ suggests that there is a lower level of potential energy available for conversion to kinetic

¹⁸¹ energy, as expected because of the weaker Ekman transport in REL.
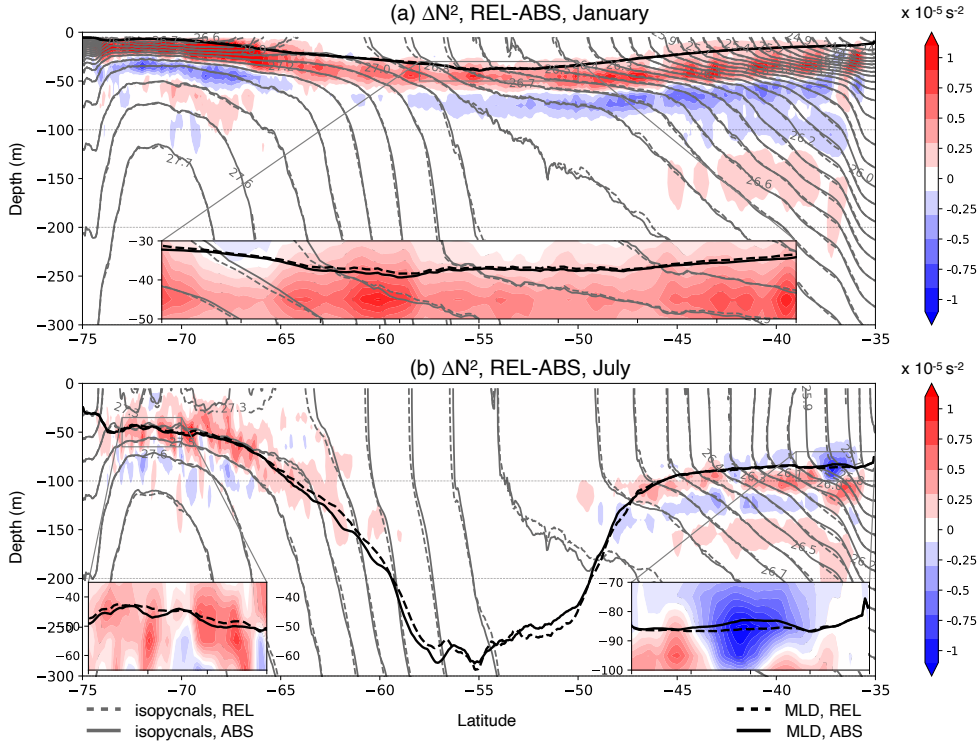
Figure 2. Shading represents the difference in the zonally averaged (from $155°W$ to $60°W$) monthly mean Brunt-Vaisälä frequency (N^2) between REL and ABS (N^2_{REL} - N^2_{ABS}) in (a) January and (b) July. The black solid/dashed lines indicate the mean MLD in ABS and REL. The ΔN^2 and the MLDs in the boxes in (a) and (b) are zoomed in on the inset plots in each panel.

3.2 Eddy kinetic energy changes

The ACC and Brazil–Malvinas Confluence Zone are known for their high level of the EKE (Wunsch, 2007), and this spatial pattern of EKE is well represented in ABS and REL with no clear seasonal variability (not shown). The difference maps of the EKE between ABS and REL show positive and negative values occurring in proximity along the ACC (Fig. 3(a,b)), probably the result of lateral shifts in mesoscale features. However, EKE is generally lower in REL than in ABL, particularly to the north of the ACC.

Indeed, the spatially averaged EKE is always lower in REL than in ABS, not only at the surface but also over the top 1000 m at all times (Fig. 4). On average, the current-wind interaction reduces the surface EKE by approximately 24%, which is slightly greater than the reduction reported in the Southern Ocean in other studies (Hutchinson et al., 2010; Munday & Zhai, 2015). Although the maximum reduction of the surface EKE oc-
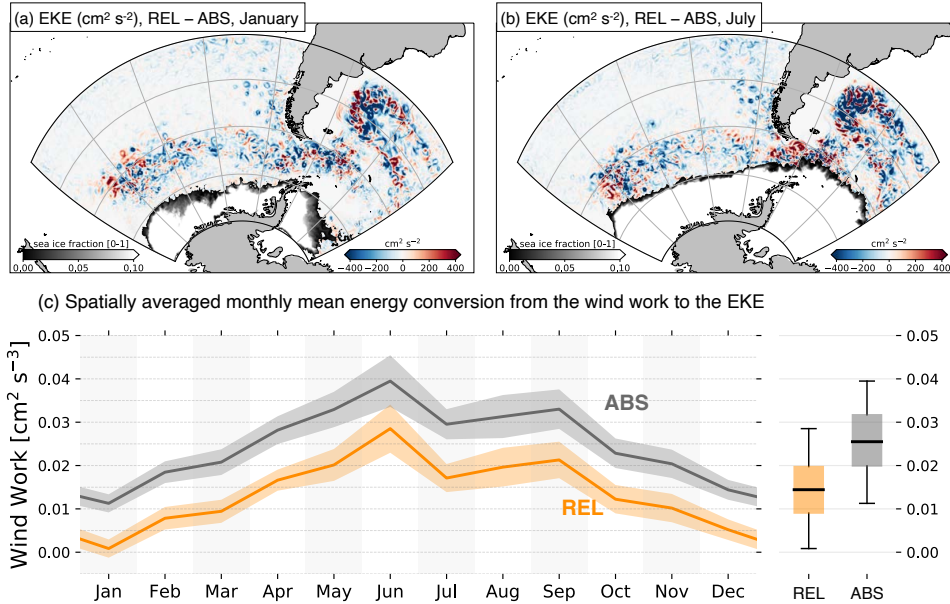
Figure 3. The difference in the monthly mean surface eddy kinetic energy (EKE, $\overline{0.5\left(u'^2 + v'^2\right)}$) computed using 5-day mean velocities in (a) January and (b) July. The sea ice fractions in the model simulation are plotted in the grayscale. In (c), the monthly mean values of the energy conversion from the wind work to the EKE along the ACC (marked by black solid lines in Fig . 1) in the ABS and REL simulations are plotted.

curs in April (up to 28%), there is no clear seasonality in the signal. The current-wind interaction alleviates overestimation of EKE in ABS, and the spatially-averaged EKE values in REL compare much better with those obtained using geostrophic current derived from the Ssalto/Duacs gridded sea level anomaly data (Fig. 4(a-c)).

A non-linear least-squares fit shows that the vertical profile of EKE in ABS decays exponentially with depth with a scale of ∼775 m. In REL, the EKE vertical profile also follows an exponential function but with a decay scale of ∼ 850 m, indicating that the EKE in REL decreases less rapidly than in ABS with depth, reflecting the more pronounced surface decrease in EKE in REL. Even though the magnitude of the reduction at depth is much smaller than those at the surface, the percentage reduction of the mean EKE reduction is still reasonably large; at 1106 m the EKE in REL is approximately 14% less than that in ABS.

(a) EKE (cm² s⁻²), AVISO

| 104 | 103 | 101 | 95 | 97 | 97 | 93 | 90 | 91 | 100 | 101 | 106 |

(b) EKE (cm² s⁻²), ABS

Depth (m)	1	2	3	4	5	6	7	8	9	10	11	12
5	130	133	135	135	129	130	125	125	126	127	128	128
15	125	128	132	131	125	124	121	121	123	123	124	123
25	124	127	130	130	123	122	119	119	121	122	122	121
35	123	126	129	129	122	120	118	118	120	121	121	120
45	122	125	129	128	121	119	117	116	118	119	120	120
55	121	125	128	127	120	118	116	115	117	118	119	119
65	120	123	127	126	120	117	115	114	116	118	118	118
75	119	122	126	125	119	116	114	114	115	117	117	117
85	117	121	124	124	118	116	114	113	115	116	116	115
95	116	119	123	122	117	115	113	112	114	115	115	114
105	115	118	121	121	115	114	112	111	113	114	114	113
116	113	116	119	119	114	112	111	110	112	113	113	112
127	112	114	117	117	112	110	109	109	111	111	112	110
140	110	112	115	115	110	109	108	107	109	110	110	108
154	108	110	113	112	107	106	105	105	107	108	108	106
172	105	107	110	109	104	103	103	103	105	106	105	104
195	101	104	106	105	100	100	100	100	102	103	102	100
223	97	99	102	100	96	95	96	96	98	99	98	96
257	93	94	96	95	91	90	91	91	94	94	93	92
300	87	89	91	89	85	85	85	86	88	89	88	86
351	82	83	84	83	79	79	79	80	82	83	82	81
410	76	77	78	77	73	73	73	74	76	77	76	75
477	70	71	72	70	67	67	67	68	70	71	70	69
553	64	65	66	64	62	61	61	62	64	65	64	63
635	58	58	59	58	56	55	55	56	58	58	58	56
722	51	52	53	52	50	49	49	50	52	52	51	50
814	46	46	47	46	44	44	44	44	46	46	45	45
910	41	41	42	41	39	39	39	39	40	41	40	39
1007	36	37	37	36	35	34	34	35	36	36	35	35
1106	32	33	33	32	31	31	30	31	32	32	31	31

(c) EKE (cm² s⁻²), REL

1	2	3	4	5	6	7	8	9	10	11	12
103	105	98	98	99	102	99	96	96	95	95	100
99	101	95	95	95	97	95	93	94	93	92	95
97	100	94	94	94	95	94	92	92	91	91	94
97	100	94	93	93	94	93	90	91	90	90	93
97	100	94	93	92	93	92	90	90	89	89	93
97	101	95	93	92	92	92	89	90	89	89	93
97	101	95	93	92	92	91	88	89	88	88	92
96	100	95	94	92	92	91	88	88	87	87	92
96	100	94	93	92	92	90	87	88	87	87	91
95	99	94	93	92	91	90	87	87	86	86	90
94	98	93	92	91	91	90	87	87	86	86	89
93	97	92	91	90	90	89	86	86	85	85	88
92	95	90	89	89	89	88	85	86	84	84	87
90	94	89	88	87	88	87	84	85	83	83	86
89	92	87	86	86	86	86	83	83	82	81	85
87	90	85	84	84	84	84	82	82	80	80	83
84	87	83	81	81	82	82	79	80	78	78	80
81	84	80	78	78	78	79	77	77	76	75	77
77	80	76	75	74	75	75	73	74	72	72	74
73	76	72	71	70	71	71	70	70	69	68	70
69	71	67	66	66	66	67	65	66	65	64	65
64	66	63	62	61	62	62	61	61	60	60	61
59	61	58	57	57	57	58	56	57	56	55	56
54	56	53	52	52	52	53	52	52	51	50	52
49	51	49	47	47	47	48	47	47	46	46	47
44	46	44	43	43	43	43	42	42	41	41	42
40	41	39	38	38	38	38	37	38	37	36	37
35	37	35	34	34	34	34	33	33	33	32	33
32	33	31	30	30	30	30	29	30	29	28	29
28	30	28	27	27	27	27	26	27	26	25	26

(d) EKE (cm² s⁻²), REL − ABS

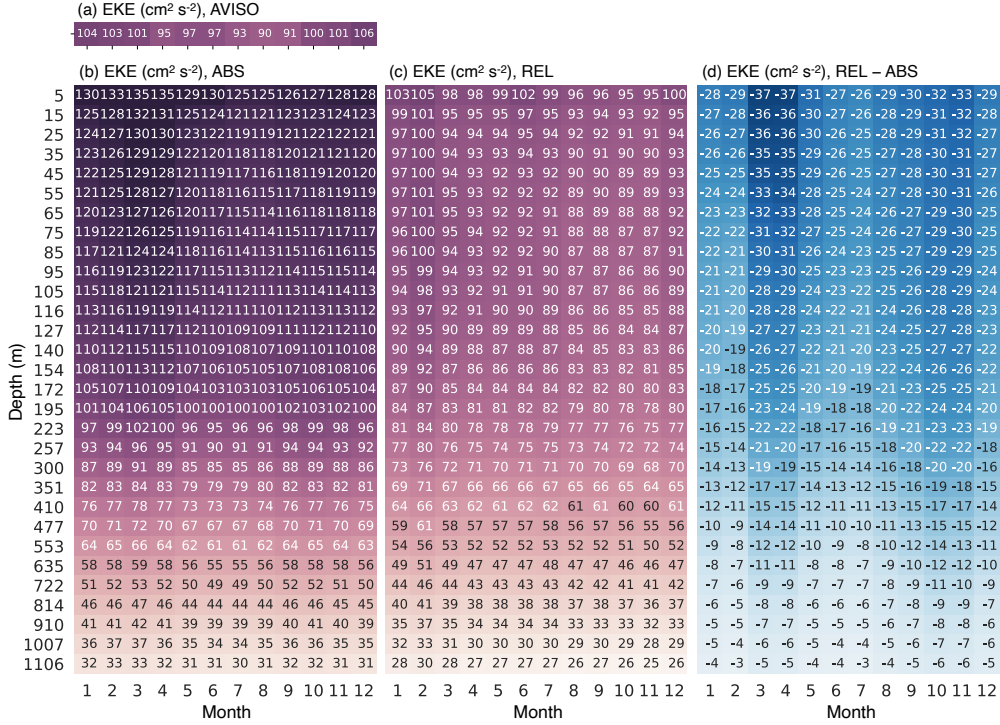| 1	2	3	4	5	6	7	8	9	10	11	12
-28	-29	-37	-37	-31	-27	-26	-29	-30	-32	-33	-29
-27	-28	-36	-36	-30	-27	-26	-28	-29	-31	-32	-28
-26	-27	-36	-36	-30	-26	-25	-28	-29	-31	-32	-27
-26	-26	-35	-35	-29	-26	-25	-27	-28	-30	-31	-27
-25	-25	-35	-35	-29	-26	-25	-27	-28	-30	-31	-27
-24	-24	-33	-34	-28	-25	-24	-27	-28	-30	-31	-26
-23	-23	-32	-33	-28	-25	-24	-26	-27	-29	-30	-25
-22	-22	-31	-32	-27	-25	-24	-26	-27	-29	-30	-25
-22	-21	-30	-31	-26	-24	-23	-25	-27	-29	-29	-25
-21	-21	-29	-30	-25	-23	-23	-25	-26	-29	-29	-24
-21	-20	-28	-29	-24	-23	-22	-25	-26	-28	-29	-24
-21	-20	-28	-28	-24	-22	-21	-24	-26	-28	-28	-23
-20	-19	-27	-27	-23	-21	-21	-24	-25	-27	-28	-23
-20	-19	-26	-27	-22	-21	-20	-23	-25	-27	-27	-22
-19	-18	-25	-26	-21	-20	-19	-22	-24	-26	-26	-22
-18	-17	-25	-25	-20	-19	-19	-21	-23	-25	-25	-21
-17	-16	-23	-24	-19	-18	-18	-20	-22	-24	-24	-20
-16	-15	-22	-22	-18	-17	-16	-19	-21	-23	-23	-19
-15	-14	-21	-20	-17	-16	-15	-18	-20	-22	-22	-18
-14	-13	-19	-19	-15	-14	-14	-16	-18	-20	-20	-16
-13	-12	-17	-17	-14	-13	-12	-15	-16	-19	-18	-15
-12	-11	-15	-15	-12	-11	-11	-13	-15	-17	-17	-14
-10	-9	-14	-14	-11	-10	-10	-11	-13	-15	-15	-12
-9	-8	-12	-12	-10	-9	-8	-10	-12	-14	-13	-11
-8	-7	-11	-11	-8	-8	-7	-9	-10	-12	-12	-10
-7	-6	-9	-9	-7	-7	-7	-8	-9	-11	-10	-9
-6	-5	-8	-8	-6	-6	-6	-7	-8	-9	-9	-7
-5	-5	-7	-7	-5	-5	-5	-6	-7	-8	-8	-6
-5	-4	-6	-6	-5	-4	-4	-5	-6	-7	-7	-6
-4	-3	-5	-5	-4	-4	-3	-4	-5	-6	-6	-5

Figure 4. (a) The monthly mean EKE at the surface averaged over the model domain calculated using AVISO product. The monthly mean EKE values as a function of month and depth in ABS and REL are shown in (b) and (c), respectively. (d) is the difference in the monthly mean EKE between ABS and REL.

The reduction of EKE in REL suggests that the energy conversion from its sources is decreased. Three major conversion processes are wind work, barotropic instability and baroclinic instability (Marchesiello et al., 2003; Seo et al., 2016; Zhan et al., 2016). We find that the reduction in EKE in REL originates primarily from reduced levels of wind work $\left(\left(\overline{u'\tau_x'} + \overline{v'\tau_y'} \right) / \rho_0 \right)$ (Fig. 3(c)). There are smaller differences in barotropic and baroclinic contributions to the EKE (not shown), consistent with previous studies. Changes in energy input from the wind are identified as the main cause of reduced EKE in previous studies (Seo et al., 2016; Oerder et al., 2018), suggesting a robustness in the impact of current-wind interaction on the energetic analysis. Reduction of the wind work is similar in each month (Fig. 3c). The annual mean reduction of the wind work is more than 40%, which is greater than that reported in the earlier work in the Southern Ocean (Hutchinson et al., 2010).

4 Impact on vertical processes

4.1 Wind-driven vertical velocity

The current-wind interaction alters not only the wind stress but also its curl, and so we anticipate modifications to the Ekman Pumping rates, w_{curl}. When relative vorticity is not negligible, as in our simulation where the Rossby number (Ro) $O(0.1)$, there is a nonlinear contribution (w_ζ) to the Ekman pumping velocity (Stern, 1965; Niiler, 1969; McGillicuddy et al., 2008; Wenegrat & Thomas, 2017). In this case the Ekman pumping velocity (w_{tot}) is given by:

$$
\begin{aligned}
w_{tot} &\approx w_{curl} + w_\zeta & (2) \\
&= \frac{\nabla \times \boldsymbol{\tau}}{\rho_0\,(f+\zeta)} + \frac{\boldsymbol{\tau} \times \nabla\zeta}{\rho_0\,(f+\zeta)^2}, & (3) \\
&= \frac{\nabla \times \boldsymbol{\tau}}{\rho_0\,(f+\zeta)} + \frac{1}{\rho_0\,(f+\zeta)^2}\left(\tau_x\frac{\partial\zeta}{\partial y} - \tau_y\frac{\partial\zeta}{\partial x}\right), & (4)
\end{aligned}
$$

where f is the Coriolis parameter and $\zeta = \partial v/\partial x - \partial u/\partial y$ is the geostrophic vorticity. According to Eq. (3), in the Southern Hemisphere where $f < 0$, a negative wind stress curl ($\nabla \times \boldsymbol{\tau}$) and a positive $\boldsymbol{\tau} \times \nabla\zeta$ result in a positive w_{tot}, i.e. upwelling.

The vertical velocity driven by wind stress curl is increased through current-wind interaction. The annual mean w_{curl} averaged over the model domain in REL is close to 0.01 m day^{-1} while it is only 0.001 m day^{-1} in ABS (Fig. 5(a)). Monthly-average w_{curl} values are always greater in REL than ABS, suggesting that there is a net upward motion induced by the interaction between the current and wind. On the other hand, the net effect of the current-wind interaction on w_ζ is downwelling (Fig. 5(b)). It moves the curve downward and the positive annual mean w_ζ in ABS becomes negative in REL. Interestingly, the net effect of current-wind interaction on w_ζ is comparable to that in w_{curl} but in the opposite direction. As a result, the change in total Ekman velocity is close to zero (not shown).

The changes in w_{curl} and w_ζ induced by current-wind interaction arise in different ways which can be understood by considering the idealized meander (Fig. 6) in which the flow is fastest at the core. The wind stress decreases near the core of the meander where the strength of the wind relative to the ocean current is at its minimum (Fig. 6(a)). As a result, the wind stress curl is negative to the north of the core and positive to the south. The resulting vertical velocities in the Southern Hemisphere ($f < 0$) are upward and downward to the north and south of the core, respectively. The strength of these
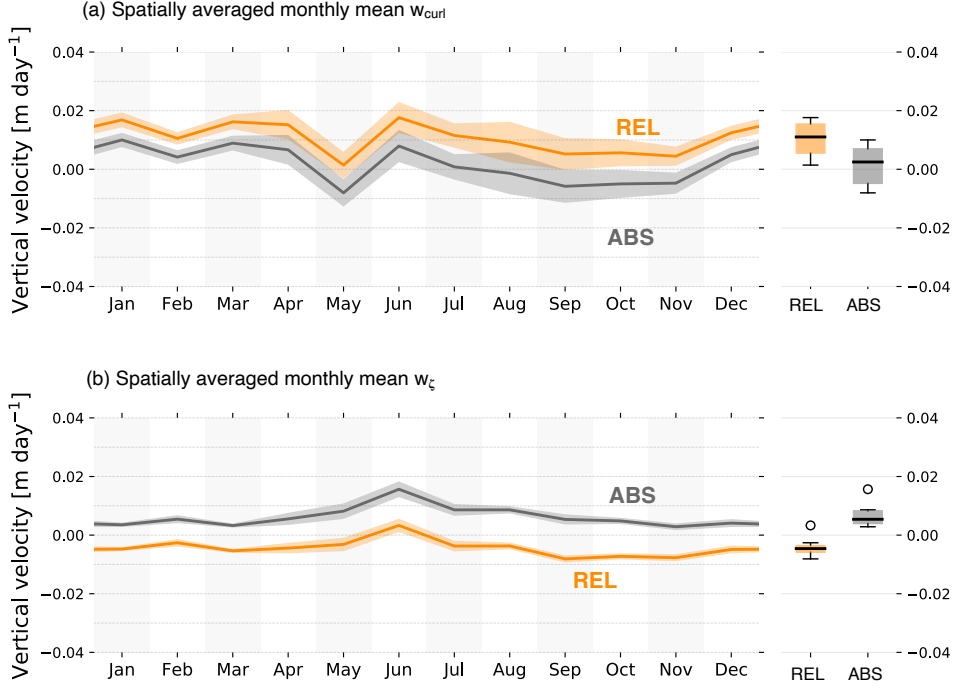
Figure 5. The monthly mean values of (a) wind-driven vertical velocity by wind stress curl (w_{curl}) and (b) lateral gradient of vorticity (w_ζ) along the ACC (marked by black solid lines in Fig . 1) in the ABS and REL simulations.

246   vertical velocities is further modified by the absolute vorticity ($f+\zeta$) according to (4)

247   because the shear of the flow in the meander creates nonzero ζ. To the north of the core,

248    $\zeta > 0$ and the upwelling becomes stronger. To the south of the core, in contrast, neg-

249   ative ζ increases the size of the absolute vorticity and weakens the downward motion.

250   Since the size of ζ is smaller than f (Ro $\sim$ O(0.1)), $f + \zeta$ in the denominator has the

251   same sign as f and so the sign of the curl-induced vertical velocity is not changed. There-

252   fore, the net vertical motion is upward in w_{curl} when the current-wind interaction is in-

253   cluded, thus accounting for Fig. 5(a).

254   When $\nabla\zeta$ is non-negligible, the horizontal shear of the flow can drive vertical mo-

255   tion (w_ζ) even in the absence of a wind stress curl. In both Northern and Southern Hemi-

256   spheres, the upward motion occurs along with the core of the meander while the periph-

257   ery is characterized by the downward motion as shown in Wenegrat and Thomas (2017)

258   and sketched in Fig. 6(b). As above, w_ζ is modified by the absolute vorticity which has

259   the opposite sign on each side of the core. Since w_ζ is inversely proportional to the square
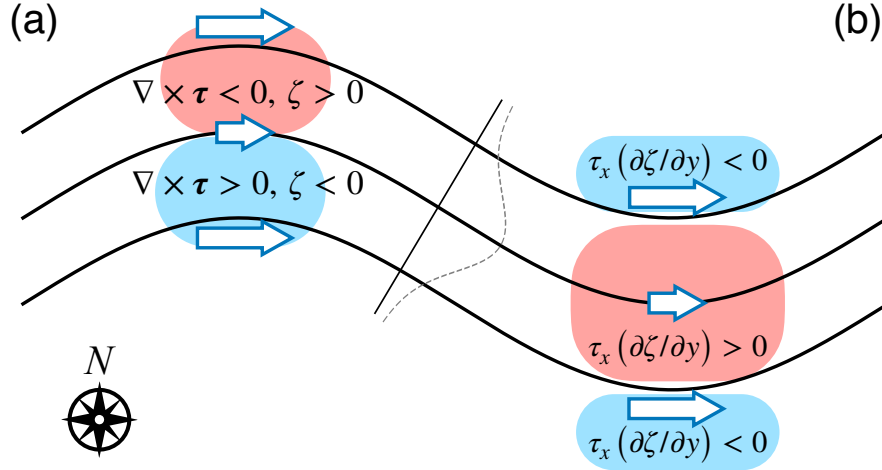
Figure 6. A diagram that visualizes the wind-driven vertical velocity estimated by (3-4) along an idealized meander enveloped by two outer black solid lines under a uniform zonal wind. The black solid line at the center represents the core axis of the meander as the current speed is shown by dashed line. The interaction between the current and wind reduces τ_x (white arrows) along the main axis of the meander. Red and blue shadings are upwelling and downwelling, respectively.

of the absolute vorticity, the impact of ζ is greater on w_ζ than on w_{curl}. But the systematic changes of w_ζ arise from the fact that the wind stress is at a minimum at the core of the meander. As explained above, the wind stress is weakest at the core of the jet where $w_\zeta > 0$, and so one can expect weakened upwelling following (4). Although the downward motion in REL is also weakened relative to ABS due to overall reduced wind stress, $(u_a - u_o)$ is smaller than that at the core, resulting in a net negative w_ζ.

If we assume that changes in w_{curl} and w_ζ due current-wind interaction are less than 100%, then scale analysis allows us to estimate expected wind-driven velocity changes. Using (1), the size of the wind stress curl can be related to the spatial changes in the current. For example, in the idealized meander system depicted in Fig. 6 with $\tau_y = 0$ and at the crest or trough where $v_o = 0$, the scale of the wind stress curl is

$$\left| \frac{\partial \tau_x}{\partial y} \right| \sim \rho_a C_D \frac{2 u_a U_o}{L}, \qquad (5)$$

271 where u_a is the zonal wind, L is the spatial scale associated with the meander, and U_o

272 measures the strength of the ocean current. The numerator of the second term in (4) can

273 be written as

$$\left| \tau_x \frac{\partial \zeta}{\partial y} \right| \sim \rho_a C_D (u_a - u_o)^2 \frac{U_o}{L^2}. \tag{6}$$

274 Then, comparing the scales of the first and the second terms in (4), one can see that

$$\left| \frac{w_{curl}}{w_\zeta} \right| = 2u_a \frac{(f + \zeta)L}{(u_a - u_o)^2}. \tag{7}$$

275 If we assume that $(u_a - u_o) \sim u_a$, and $(f + \zeta) \sim f$, (7) approaches 1 for $f = 10^{-4}$

276 s^{-1}, $L = 50$ km and $u_a = 10$ m s^{-1}, indicating that the changes in w_{curl} and w_ζ are

277 similar.

278 The real Southern Ocean differs from our idealized system since asymmetric crests

279 and troughs and well-developed eddies populate the ACC. Furthermore, the surface wind

280 is not constant in time and space, adding yet more complexity. Sea surface temperature

281 also varies spatially, especially near fronts, eddies and meanders, affecting the wind in

282 the planetary boundary layer through the changes in the vertical turbulent mixing (Chelton

283 et al., 2004; Seo et al., 2007; Byrne et al., 2015, 2016), increasing the complexity of the

284 real system. Nevertheless, the changes in w_{curl} and w_ζ observed in Fig. 5 are consistent

285 with the insights obtained from consideration of our idealized meander.

286 ### 4.2 Vertical Mixing

287 The impact of current-wind interaction on near-surface vertical mixing is also of

288 interest. Observations reveal large seasonality in the MLD, ranging from less than 100

289 m in austral summer to more than 500 m in austral winter in the study area (Dong et

290 al., 2008). Our simulations, both ABS and REL, capture the large seasonal and spatial

291 variability exhibited by MLD, as well as its modulation by mesoscale eddies - see Haus-

292 mann et al (2017). For example, summertime MLD in REL is generally shallower than

293 50 m except to the north of the ACC where the MLD reaches 70 m or so (Fig. 7(a)). In

294 winter, the MLD is generally deeper near the northern boundary of the ACC, particu-

295 larly in the Pacific sector, exceeding 500 m in REL (Fig. 7(b)), which is consistent with

296 observations.

297 The impact of the current-wind interaction on the local MLD can exceed 100 m,

298 but it does not induce a coherent large-scale pattern of change in MLD. Differences are
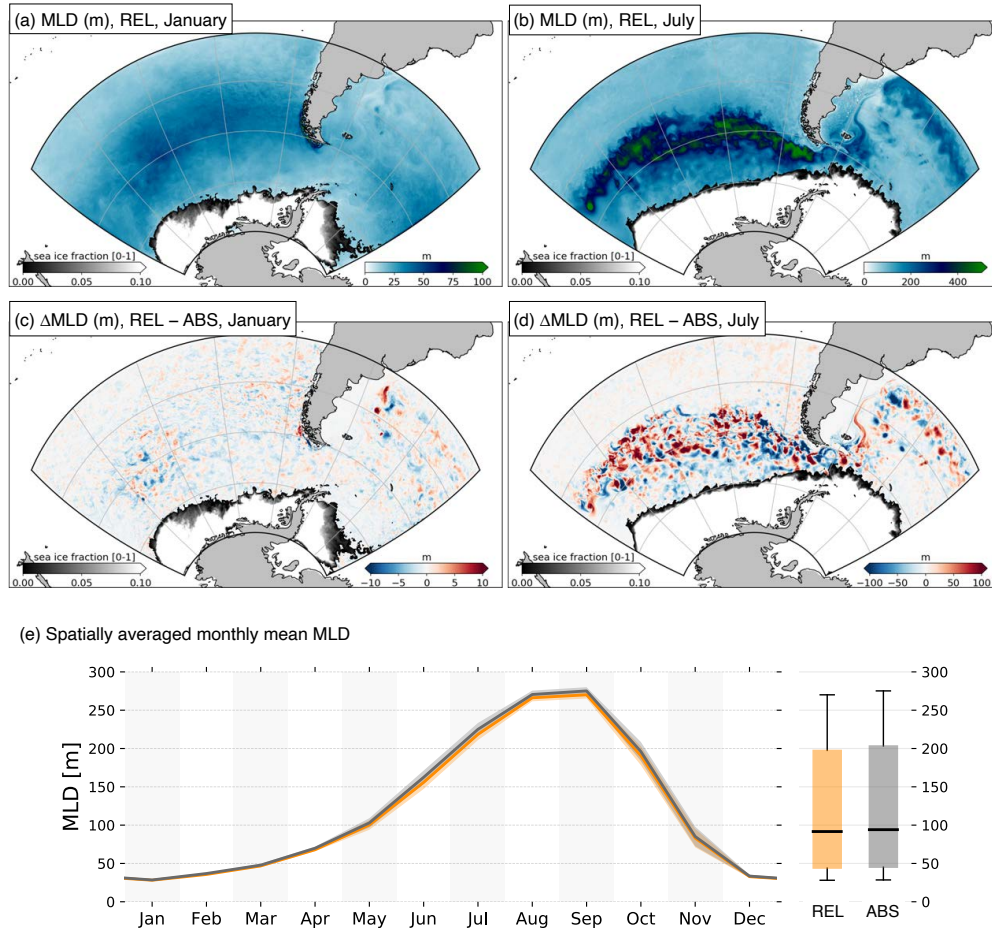
Figure 7. Monthly averaged mixed layer depth (MLD) in REL for (a) January and (b) July. The MLD differences between REL and ABS for those months are shown in (c) and (d), respectively. (e) shows the monthly mean MLD along the ACC in REL (orange) and ABS (gray).

299   shown in Fig. 7(c,d) and exhibit both positive and negative values on spatial scales sim-

300   ilar to the mesoscale ($O(10-100km)$). Although the patchiness in the differences may

301   be due to the relatively short integration of the model, it suggests that MLD changes

302   are mainly due to the shift of the meander and eddy locations in both seasons. For ex-

303   ample, the MLD anomalies associated with mesoscale eddies in this region average a few

304   tens of meters in winter (Song et al., 2015; Hausmann et al., 2017). If REL and ABS have

305   mesoscale eddies with opposite polarity at the same location, MLD differences between

306   them can easily exceed 100 m (Fig. 7(d)). In summer, observed MLD anomalies asso-

307   ciated with mesoscale eddies are less than 10 m (Hausmann et al., 2017), comparable to

308   the MLD differences between the two simulations (Fig. 7(c)). These positive and neg-

309 ative MLD anomalies are generally canceled out in the spatial average so that the monthly-

310 mean MLD curves are very similar between the two simulations. A careful examination,

311 however, reveals that MLD in REL is a few meters shallower than ABS (Fig. 7(e)).

312   The KPP vertical mixing scheme used in our simulations determines the mixing

313 depth based on a Richardson number defined by the ratio between the Brunt-Väisälä fre-

314 quency (N^2) and the vertical shear of the flow. Thus small differences in MLD suggest

315 that the Richardson numbers are rather similar in ABS and REL. To quantify, we first

316 compute the rotary power spectral density of the vertical shear of the ocean currents at

317 105 m in both the ABS and REL runs in September (Fig. 8). Two frequency bands show

318 elevated power in both ABS and REL: one near zero associated with the geostrophic com-

319 ponent, the other near the inertial frequency (f) in the positive frequency domain (Fig.

320 8(a,b)). The elevated power near the frequency of the local f (dotted line in Fig. 8) in-

321 dicates that both simulations capture the near-inertial waves that are important in ver-

322 tical mixing. In the Southern Hemisphere, near-inertial waves drive counterclockwise ro-

323 tation with near-inertial frequency creating vertical shear and enhancing vertical mix-

324 ing (Alford et al., 2016). Hence the ability to resolve near-inertial waves has a big im-

325 pact on MLD in our numerical simulations (Jochum et al., 2013; Song et al., 2019). Al-

326 though a careful examination shows slightly less power in REL (Fig. 8(c)), both simu-

327 lations clearly resolve near-inertial waves, indicating that the current-wind interaction

328 does not significantly alter the generation of near-inertial waves. Although stratification

329 changes are not significant within the mixed layer, there is a systematic increase of N^2

330 at the base of the mixed layer, as described below.

4.3 Stratification

332   Current-wind interaction causes change in the upper ocean stratification with in-

333 creased N^2 at the bottom of the mixed layer (Fig. 2). This pattern is more pronounced

334 in the summer, when N^2 in ABS is roughly 10% higher than N^2 in REL (Fig. 2(a)). This

335 increase of N^2 is likely a result of weakening of wind-driven Ekman transport. Ekman

336 transport is weaker in REL because the wind stress is weaker (Fig. 1). As a result, the

337 outcropping positions of the isopycnals in REL are further south than those in ABS. At

338 the depth where the direct impact of the wind stress becomes small, isopycnals in REL

339 and ABS converge. Hence the slopes of isopycnals in REL are more gradual than in ABS

340 when connecting the isopycnals at the surface to depth.

Rotary power spectral density (PSD) of d**u**/dz at 105 m, September
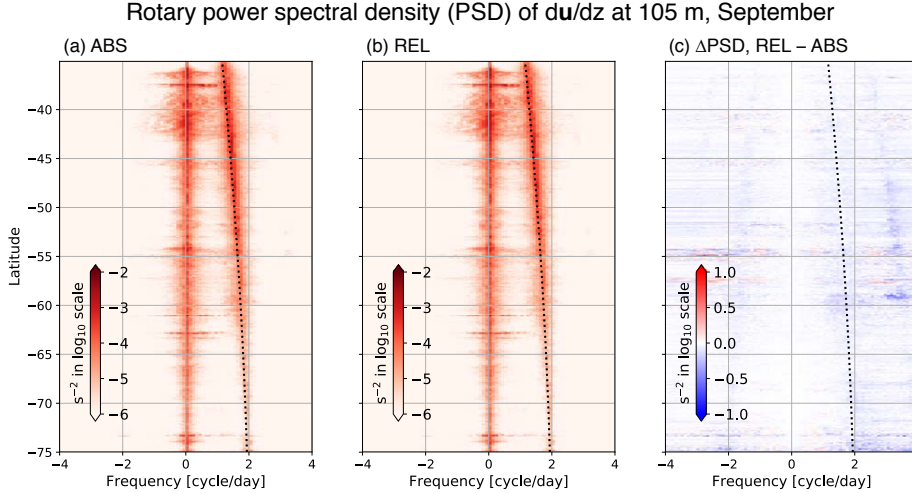
Figure 8. Rotary power spectral density of the ocean current vertical shear at 105 m in September as a function of frequency and latitude for (a) ABS and (b) REL. The rotary power spectral analysis reveals motions rotating in both counterclockwise (positive frequencies) and clockwise (negative frequencies). (c) is the difference between (a) and (b). The color represents the intensity. The dotted lines indicate the inertial frequency at each latitude.

One might anticipate a decrease in MLD in REL based on the enhanced stratification, especially in austral summer. Although a closer inspection indicates that the MLD (black thick lines in Fig. 2) is slightly shallower in REL, it generally remains unchanged as the increase of N^2 occurs largely below the mixed layer.

In winter when vertical mixing homogenizes the surface layer, the background N^2 is already small and isopycnals are almost vertical near the surface. Although the isopycnals are shifted poleward near the surface in REL due to the weaker wind stress, the interaction between the current and wind does not alter stratification as much as in summer, perhaps because of the absence of a well-developed thermocline. This is particularly true near the ACC, showing no changes in N^2 (Fig. 2(b)). However, the tendency for an N^2 increase near the bottom of the mixed layer remains, suggesting that the current-wind interaction tends to increase the stratification at the base of the mixed layer.

5 Discussion and Conclusion

Ocean currents are often neglected in the calculation of wind stress because typically surface current speeds are one order of magnitude smaller than the 10 m wind. However, previous studies have shown that the presence of ocean currents can have a nonnegligible effect on wind stress and the ocean's EKE. In the Southern Ocean, numerical studies with idealized models report that current-wind interaction reduces the EKE by up to 18% (Hutchinson et al., 2010; Munday & Zhai, 2015). Indeed satellite observations suggest that the impact of current-wind interaction is especially large in the Southern Ocean (Renault, McWilliams, & Masson, 2017). Here, we have extended the investigation of current-wind interaction to explore its impact on vertical processes such as wind-driven vertical velocity and vertical mixing using a 0.05° resolution model encompassing the Drake passage.

Our experiment shows a 24% reduction in surface EKE using the relative wind stress. As a result, the EKE bias in the simulations with absolute wind is alleviated. The size of the EKE reduction is somewhat larger than reported in previous idealised studies, possibly due to the increased resolution employed here. The EKE reduction is not limited to the surface but extends to depths of 1000 m or more where EKE is reduced by 13%. The effect also persists throughout the year. An energy budget analysis shows that the reduced EKE is a consequence of a weaker wind work.

The wind-induced vertical velocity is also modified by the interaction. By consideration of an idealized meandering jet system in the southern hemisphere ($f < 0$), one can anticipate that positive relative vorticity in a meander crest will amplify upward motion, while negative relative vorticity in a meander trough will weaken downward motion. The overall contribution from the wind stress curl created by the current-wind interaction is therefore one of upwelling. On the other hand, nonlinear contributions to the wind-driven vertical velocity (w_ζ) induce a net downward motion due to the interaction. Near the core of the jet where $\nabla \zeta$ is positive, upwelling occurs which contrasts with downwelling outside of the jet. If the ocean current is taken in to account in the wind stress calculation, the wind stress over the core of the jet becomes weaker than outside, leading to a net negative change in w_ζ. Interestingly, the changes in w_{curl} and w_ζ compensate each other, such that the net changes in the wind-driven vertical velocity are rather small in our simulation.

385   One may anticipate a shoaling of the MLD in REL since both the momentum trans-

386   fer from the atmosphere and EKE are reduced. In our experiment, however, the MLD

387   shows only modest changes in the spatial mean. The magnitude of MLD anomalies are

388   considerable in some locations, but this is the result of the shift of locations of mean-

389   ders and eddies. Further analysis shows that there are no significant changes in the ver-

390   tical shear of the flow and stratification within the mixed layer, leading to little change

391   in the Richardson number. Interestingly, the rotary power spectral density functions of

392    $d\mathrm{u}/dz$ shows little difference between ABS and REL, which suggests that the near-inertial

393   waves have similar amplitude in both cases and hence there is no modulation of shear-

394   induced mixing. In the K-profile parameterization used in our simulations, the mixing

395   depth is determined by the Richardson number, which may explain why there are rather

396   small net MLD changes caused by current-wind interaction. It is possible that vertical

397   mixing schemes based on turbulent kinetic energy budgets may induce a shoaling of the

398   MLD.

399   Another factor that may lead to insensitivity of the MLD is the influence of the

400   upstream open boundary condition. In our study area, the eastward flow constantly en-

401   ters from the western boundary (160°W), feeding the same water mass to the interior

402   of ABS and REL. This eastward flow includes the ACC that can be up to 50 cm s^{-1}.

403   It then takes roughly only 180 days to exit downstream (20°W). Hence, even if the current-

404   wind interaction were to modify the MLD, inflow from the upstream boundary contin-

405   uously resets the water properties in ABS and REL to the values at the western bound-

406   ary condition, possibly leading to smaller MLD changes.

407   Below the mixed layer there is a clear increase in stratification due to current-wind

408   interaction. In summer, there is a roughly 10% increase of the Brunt-Väisälä frequency

409   (N^2) in REL over a few tens of meters. Although this tendency is attenuated in winter,

410   it remains in the thermocline. The current-wind interaction reduces overall eastward wind

411   stress to the ocean, leading to a weaker equatorward Ekman transport. Isopycnals thus

412   outcrop further south in REL while their latitudinal position below the Ekman layer is

413   barely changed. As a result, the slopes of isopycnals in REL are more gradual than those

414   in ABS, yielding enhanced stratification below the mixed layer.

415   This result may appear to contradict the conclusion of Munday and Zhai (2015)

416   in which the isopycnals become steeper when the wind stress is calculated using both

10 m wind and ocean current (relative wind stress) in an idealized channel model. In their analysis, however, the simulation is compared with an absolute wind stress reference in which the wind stress is calculated using a 10 m wind adjusted to have the same mean value as the relative wind stress simulation. This ensures that the Ekman transport is unchanged. In contrast, our study allows the wind stress to deviate. Another possible explanation is that we report the response to changes over a timescale of a few years, whilst their study documented the multi-decadal change.

Future work will address the biogeochemical implications of our findings, as biological and chemical processes can be sensitive to subtle changes in ocean physics due to their intrinsic nonlinearity. Specifically, changes in stratification and upwelling rates can modulate biogeochemical processes in the Southern Ocean due to lack of iron and light available for the primary production (Boyd et al., 1999, 2000; Venables & Moore, 2010). In addition to supply of iron through dust deposition, sediment, and sea-ice melt, vertical mixing is an important process since it entrains iron-rich subsurface waters (Boyd & Ellwood, 2010; Tagliabue et al., 2014). In summer when light is abundant, satellite observations and eddy-rich biogeochemical simulations show a positive correlation between anomalies of sea level and chlorophyll, suggesting that anomalously deep vertical mixing increases the iron supply and primary production (Song et al., 2018). Hence increased stratification in the thermocline induced by current-wind interaction may make entrainment of iron-rich water more sporadic thus suppressing primary productivity.

Current-wind interaction can also influence air-sea carbon dioxide (CO_2) exchange. Dissolved inorganic carbon (DIC), whose concentration increases poleward in the Southern Ocean, may have lower surface concentrations under weaker Ekman transport with the relative wind stress in both summer and winter. This could cause reduction in the partial pressure of CO_2 (pCO_2), leading to more CO_2 uptake in summer and less outgassing in winter. On the other hand, there may be a decrease in the biological drawdown of CO_2 in summer as discussed above, which would counterbalance the changes in the Ekman transport. Hence it is necessary to thoroughly investigate the impact of the current-wind interaction on the carbon cycle in the Southern Ocean.

Acknowledgments

References

Adcroft, A., Hill, C., Campin, J.-M., Marshall, J., & Heimbach, P. (2004). Overview of the formulation and numerics of the MIT GCM. In *Proceedings of the ECMWF Seminar Series on Numerical Methods, Recent Developments in Numerical Methods for Atmosphere and Ocean Modelling* (pp. 139–149). ECMWF.

Adcroft, A. J., Hill, C. N., & Marshall, J. (1997). Representation of topography by shaved cells in a height coordinate ocean model. *Mon. Wea. Rev.*, *125*, 2293–2315.

Alford, M. H., MacKinnon, J. A., Simmons, H. L., & Nash, J. D. (2016). Near-Inertial Internal Gravity Waves in the Ocean. *Annu. Rev. Mar. Sci.*, *8*(1), 95–123. doi: 10.1146/annurev-marine-010814-015746

Boyd, P. W., & Ellwood, M. J. (2010). The biogeochemical cycle of iron in the ocean. *Nature Geosci.*, *3*, 675–682.

Boyd, P. W., LaRoche, J., Gall, M., Frew, R., & McKay, R. M. L. (1999). Role of iron, light, and silicate in controlling algal biomass in subantarctic waters S. E. of New Zealand. *J. Geophys. Res.*, *104*(C6), 13395–13408. doi:

481   10.1029/1999JC900009

482   Boyd, P. W., Watson, A. J., Law, C. S., Abraham, E. R., Trull, T., Murdoch, R.,

483   . . . Zeldis, J. (2000, October). A mesoscale phytoplankton bloom in the polar

484   Southern Ocean stimulated by iron fertilization. *Nature*, *407*(6805), 695–702.

485   Byrne, D., Münnich, M., Frenger, I., & Gruber, N. (2016). Mesoscale atmosphere

486   ocean coupling enhances the transfer of wind energy into the ocean. *Nat Com-*

487   *mun*, *7*, ncomms11867. doi: 10.1038/ncomms11867

488   Byrne, D., Papritz, L., Frenger, I., Münnich, M., & Gruber, N. (2015). Atmo-

489   spheric Response to Mesoscale Sea Surface Temperature Anomalies: As-

490   sessment of Mechanisms and Coupling Strength in a High-Resolution Cou-

491   pled Model over the South Atlantic. *J. Atmos. Sci.*, *72*, 1872–1890. doi:

492   10.1175/JAS-D-14-0195.1

493   Chelton, D. B., DeSzoeke, R., Schlax, M., Naggar, K. E., & Siwertz, N. (1998).

494   Geographical variability of the first baroclinic rossby radius of deformation. *J.*

495   *Phys. Oceanogr.*, *28*, 433–460.

496   Chelton, D. B., Schlax, M. G., Freilich, M. H., & Milliff, R. F. (2004). Satellite Mea-

497   surements Reveal Persistent Small-Scale Features in Ocean Winds. *Science*,

498   *303*(5660), 978–983.

499   Dawe, J. T., & Thompson, L. (2006). Effect of ocean surface currents on wind stress,

500   heat flux, and wind power input to the ocean. *Geophys. Res. Lett.*, *33*(9).

501   de Boyer Montégut, C., Madec, G., Fischer, A. S., Lazar, A., & Iudicone, D.

502   (2004). Mixed layer depth over the global ocean: An examination of profile

503   data and a profile-based climatology. *J. Geophys. Res.*, *109*, C12003. doi:

504   10.1029/2004JC002378

505   Dewar, W. K., & Flierl, G. R. (1987). Some Effects of the Wind on Rings. *J. Phys.*

506   *Oceanogr.*, *17*, 1653–1667.

507   Dohan, K., & Maximenko, N. (2010). Monitoring ocean currents with satellite sen-

508   sors. *Oceanography*, *23*(4), 94–103. doi: 10.5670/oceanog.2010.08

509   Dong, S., Sprintall, J., Gille, S. T., & Talley, L. (2008). Southern Ocean mixed-layer

510   depth from Argo float profiles. *J. Geophys. Res.*, *113*, C06013.

511   Duhaut, T. H. A., & Straub, D. N. (2006). Wind stress dependence on ocean sur-

512   face velocity: Implications for mechanical energy input to ocean circulation. *J.*

513   *Phys. Oceanogr.*, *36*, 202–211. doi: https://doi.org/10.1175/JPO2842.1

514 Eden, C., & Dietze, H. (2009). Effects of mesoscale eddy/wind interactions on
515 biological new production and eddy kinetic energy. *J. Geophys. Res., 114*,
516 C05023. doi: 10.1029/2008JC005129

517 Forget, G. (2010). Mapping ocean observations in a dynamical framework: A 2004-
518 06 ocean atlas. *J. Phys. Oceanogr., 40*(6), 1201–1221.

519 Hausmann, U., McGillicuddy, D. J., & Marshall, J. (2017). Observed mesoscale
520 eddy signatures in Southern Ocean surface mixed-layer depth. *J. Geophys.*
521 *Res. Oceans,, 122*(1), 617–635. doi: 10.1002/2016JC012225

522 Holte, J., & Talley, L. (2009). A New Algorithm for Finding Mixed Layer Depths
523 with Applications to Argo Data and Subantarctic Mode Water Formation. *J.*
524 *Atmos. Oceanic Technol., 26*(9), 1920–1939.

525 Hutchinson, D. K., Hogg, A. M. C., Blundell, J. R., Hutchinson, D. K., Hogg,
526 A. M. C., & Blundell, J. R. (2010). Southern Ocean Response to Relative
527 Velocity Wind Stress Forcing. *J. Phys. Oceanogr., 40*(2), 326–339.

528 Jochum, M., Briegleb, B. P., Danabasoglu, G., Large, W. G., Norton, N. J., Jayne,
529 S. R., . . . Bryan, F. O. (2013). The impact of oceanic near-inertial waves on
530 climate. *J. Climate, 26*, 2833–2844.

531 Large, W. G., McWilliams, J., & Doney, S. (1994). Oceanic vertical mixing: A re-
532 view and a model with nonlocal boundary layer parameterization. *Rev. Geo-*
533 *phys., 32*(4), 363–403.

534 Large, W. G., & Yeager, S. G. (2004). Diurnal to decadal global forcing for ocean
535 and sea-ice models: the data sets and flux climatologies. In *Ncar technical*
536 *note: Ncar/tn-460+str.* CGD Division of National Center for Atmospheric
537 Research Boulder.

538 Laurindo, L. C., Mariano, A. J., & Lumpkin, R. (2017). An improved near-surface
539 velocity climatology for the global ocean from drifter observations. *Deep-Sea*
540 *Res. I, 124*, 73 - 92. doi: https://doi.org/10.1016/j.dsr.2017.04.009

541 Marchesiello, P., McWilliams, J. C., & Shchepetkin, A. (2003). Equilibrium struc-
542 ture and dynamics of the California Current System. *J. Phys. Oceanogr., 33*,
543 753–783. doi: 10.1175/1520-0485(2003)33,753:ESADOT.2.0.CO;2

544 Marshall, J., Adcroft, A., Hill, C., Perelman, L., & Heisey, C. (1997). A finite-
545 volume, incompressible Navier Stokes model for studies of the ocean on parallel
546 computers. *J. Geophysical Res., 102*(C3), 5753–5766.

Marshall, J., Hill, C., Perelman, L., & Adcroft, A. (1997). Hydrostatic, quasi-hydrostatic, and nonhydrostatic ocean modeling. *J. Geophys. Res.*, *102*(C3), 5733–5752.

Marshall, J., Jones, H., & Hill, C. (1998). Efficient ocean modeling using non-hydrostatic algorithms. *J. Mar. Syst.*, *18*, 115–134.

Maximenko, N., Niiler, P., Rio, M., Melnichenko, O., Centurioni, L., Chambers, D., . . . Galperin, B. (2009). Mean dynamic topography of the ocean derived from satellite and drifting buoy data using three different techniques. *J. Atmos. Ocean. Technol.*, *26*, 1910–1918.

McGillicuddy, D. J., Ledwell, J., & Anderson, L. (2008). Response to comments on "eddy/wind interactions stimulate extraordinary mid-ocean plankton blooms.". *Sciences*, *320*, 488. doi: 10.1126/science.1148974

Munday, D. R., & Zhai, X. (2015). Sensitivity of Southern Ocean circulation to wind stress changes: Role of relative wind stress. *Ocean Modell.*, *95*, 15–24.

Niiler, P. P. (1969). On the Ekman divergence in an oceanic jet. *J. Geophys. Res.*, *74*, 7048–7052. doi: 10.1029/JC074i028p07048

Oerder, V., Colas, F., Echevin, V., Masson, S., & Lemarié, F. (2018). Impacts of the Mesoscale Ocean-Atmosphere Coupling on the Peru-Chile Ocean Dynamics: The Current-Induced Wind Stress Modulation. *J. Geophys. Res. Oceans*, *123*, 812–833. doi: https://doi.org/10.1002/2017JC013294

Renault, L., McWilliams, J. C., & Masson, S. (2017). Satellite Observations of Imprint of Oceanic Current on Wind Stress by Air-Sea Coupling. *Sci. Rep.*, *7*(1), 17747.

Renault, L., McWilliams, J. C., & Penven, P. (2017). Modulation of the Agulhas Current Retroflection and Leakage by Oceanic Current Interaction with the Atmosphere in Coupled Simulations. *J. Phys. Oceanogr.*, *47*(8), 2077–2100.

Renault, L., Molemaker, M. J., Gula, J., Masson, S., & McWilliams, J. C. (2016). Control and stabilization of the Gulf Stream by oceanic current interaction with the atmosphere. *J. Phys. Oceanogr.*, *46*, 3439 – 3453.

Renault, L., Molemaker, M. J., McWilliams, J. C., Shchepetkin, A. F., Lemarié, F., Chelton, D., . . . Hall, A. (2016). Modulation of wind work by oceanic current interaction with the atmosphere. *J. Phys. Oceanogr.*, *46*, 1685–1704.

Seo, H. (2017). Distinct Influence of Air–Sea Interactions Mediated by Mesoscale

Sea Surface Temperature and Surface Current in the Arabian Sea. *J. Climate*, *30*(20), 8061–8080.

Seo, H., Jochum, M., Murtugudde, R., Miller, A. J., & Roads, J. O.   (2007).   Feed-back of Tropical Instability-Wave-Induced Atmospheric Variability onto the Ocean. *J. Climate*, *20*(23), 5842–5855.

Seo, H., Miller, A. J., & Norris, J. R.   (2016).   Eddy–wind interaction in the California Current System: Dynamics and impacts.   *J. Phys. Oceanogr.*, *46*(2), 439–459. doi: doi:10.1175/JPO-D-15-0086.1

Seo, H., Subramanian, A. C., Song, H., & Chowdary, J. S.   (2019).   Coupled effects of ocean current on wind stress in the Bay of Bengal: Eddy energetics and upper ocean stratification.   *Deep-Sea Res. II*.   doi: https://doi.org/10.1016/j.dsr2.2019.07.005

Simmons, A., Uppala, S., Dee, D., & Kobayashi, S.   (2007).   ERA-Interim: New ECMWF reanalysis products from 1989 onwards.   In *Ecmwf newsletter* (Vol. 110, pp. 25–35). ECMWF.

Song, H., Long, M. C., Gaube, P., Frenger, I., Marshall, J., & McGillicuddy, D. (2018). Seasonal variation in the correlation between anomalies of sea level and chlorophyll in the antarctic circumpolar current.   *Geophys. Res. Lett.*, *45*(10), 5011–5019. doi: 10.1029/2017GL076246

Song, H., Marshall, J., Campin, J.-M., & McGillicuddy, D. J.   (2019).   Impact of near-inertial waves on vertical mixing and air-sea CO_2 fluxes in the Southern Ocean.   *J. Geophys. Res. Oceans*, *124*, 4605–4617.   doi: https://doi.org/10.1029/2018JC014928

Song, H., Marshall, J., Gaube, P., & McGillicuddy, D. J.   (2015).   Anomalous chlorofluorocarbon uptake by mesoscale eddies in the Drake Passage region.   *J. Geophys. Res. Oceans*, *120*, 1065–1078. doi: 10.1002/2014JC010292

Song, H., Marshall, J., Munro, D. R., Dutkiewicz, S., Sweeney, C., McGillicuddy, D. J., & Hausmann, U.   (2016).   Mesoscale modulation of air-sea CO_2 flux in Drake Passage.   *J. Geophys. Res. Oceans*, *121*, 6635–6649.   doi: 10.1002/2016JC011714

Stern, M.   (1965).   Interaction of a uniform wind stress with a geostrophic vortex. *Deep-Sea Res. Oceanogr. Abstr.*, *12*, 355–367. doi: 10.1016/0011-7471(65)90007-0

Tagliabue, A., Sallée, J.-B., Bowie, A. R., Lévy, M., Swart, S., & Boyd, P. W. (2014). Surface-water iron supplies in the Southern Ocean sustained by deep winter mixing. *Nature Geosci.*, *7*, 314–320. doi: 10.1038/ngeo2101

Talley, L. D., Pickard, G. L., Emery, W. J., & Swift, J. H. (2011). *Descriptive physical oceanography: An introduction* (6th ed.). Academic Press.

Tsujino, H., Urakawa, S., Nakano, H., Small, R. J., Kim, W. M., Yeager, S. G., ... Yamazaki, D. (2018). Jra-55 based surface dataset for driving ocean-sea-ice models (jra55-do). *Ocean Modell.*, *130*, 79 - 139. doi: https://doi.org/10.1016/j.ocemod.2018.07.002

Tulloch, R., Ferrari, R., Jahn, O., Klocker, A., LaCasce, J., Ledwell, J., ... Watson, A. (2014). Direct estimates of lateral eddy diffusivity upstream of Drake Passage. *J. Phys. Oceanogr.*, *44*, 2593–2616.

Tulloch, R., Marshall, J., Hill, C., & Smith, K. S. (2011). Scales, growth rates, and spectral fluxes of baroclinic instability in the ocean. *J. Phys. Oceanogr.*, *41*(6), 1057-1076. doi: 10.1175/2011JPO4404.1

Venables, H., & Moore, C. M. (2010). Phytoplankton and light limitation in the southern ocean: Learning from high-nutrient, high-chlorophyll areas. *J. Geophys. Res.*, *115*, C02015. doi: 10.1029/2009JC005361

Wenegrat, J. O., & Thomas, L. N. (2017). Ekman Transport in Balanced Currents with Curvature. *J. Phys. Oceanogr.*, *47*, 1189–1203. doi: 10.1175/JPO-D-16-0239.1

Wunsch, C. (2007). The past and future ocean circulation from a contemporary perspective. In A. Schmittner, J. C. Chiang, & S. R. Hemming (Eds.), *Ocean circulation: Mechanisms and impacts–past and future changes of meridional overturning* (p. 53-74). American Geophysical Union (AGU). doi: 10.1029/173GM06

Zhai, X., & Greatbatch, R. J. (2007). Wind work in a model of the northwest Atlantic Ocean. *Geophys. Res. Lett.*, *34*, L04606. doi: 10.1029/2006GL028907

Zhai, X., Johnson, H. L., Marshall, D. P., & Wunsch, C. (2012). On the Wind Power Input to the Ocean General Circulation. *J. Phys. Oceanogr.*, *42*(8), 1357–1365.

Zhan, P., Subramanian, A. C., Yao, F., Kartadikaria, A. R., Guo, D., & Hoteit, I. (2016, July). The eddy kinetic energy budget in the Red Sea. *J. Geophys. Res.*

646   *Oceans*, *121*(7), 4732–4747.